

Quantum gate teleportation between separated zones of a trapped-ion processor

Yong Wan,^{1,2*†} Daniel Kienzler,^{1,2‡} Stephen D. Erickson,^{1,2} Karl H. Mayer,^{1,2}
 Ting Rei Tan,^{1,2‡} Jenny J. Wu,^{1,2} Hilma M. Vasconcelos,^{1,2,4} Scott Glancy,¹
 Emanuel Knill,¹ David J. Wineland,^{1,2,3} Andrew C. Wilson,¹ Dietrich
 Leibfried¹

¹National Institute of Standards and Technology, 325 Broadway, Boulder, CO
 80305, USA

²Department of Physics, University of Colorado, Boulder, CO 80309, USA

³Department of Physics, University of Oregon, Eugene, OR 97403, USA

⁴Departamento de Engenharia de Teleinformática, Universidade Federal do
 Ceará, Fortaleza, Brazil

*To whom correspondence should be addressed. E-mail: yong.wan@nist.gov.

[†]These authors contributed equally to this work. [‡]Current address: ETH
 Zurich, Otto-Stern-Weg 1, HPF E10, 8093 Zurich, Switzerland (D.K.); Centre
 for Quantum Technologies, 3 Science Drive 2, 117543 Singapore (T.R.T.).

July 3, 2022

Large-scale quantum computers will inevitably require quantum gate operations between widely separated qubits, even within a single quantum information processing device. Nearly two decades ago, Gottesman and Chuang proposed a method for implementing such operations, known as quantum gate teleportation (1). It requires only local operations on the remote qubits, classical communication, and shared entanglement that is prepared before the

logical operation. Here we demonstrate this approach in a scalable architecture by deterministically teleporting a controlled-NOT (CNOT) gate between two computational qubits in spatially separated zones in a segmented ion trap. Our teleported CNOT's entanglement fidelity is in the interval $[0.845, 0.872]$ at the 95% confidence level. The implementation combines ion shuttling with individually-addressed single-qubit rotations and detections, same- and mixed-species two-qubit gates, and real-time conditional operations, thereby demonstrating essential tools for scaling trapped-ion quantum computers combined in a single device.

Quantum computers have the potential to solve certain problems that are intractable using conventional computers. However, beyond the relatively simple quantum algorithms that can be currently realized, many quantum bits (qubits) are required to outperform conventional computing capabilities, and scaling quantum computers to be practically useful is difficult (2). As the system size increases, the average distance between qubits grows as well, making it much harder to connect arbitrary qubits. Quantum mechanics offers a unique solution, known as *gate teleportation*, where logical gates are implemented between spatially separated qubits (1, 3). In this approach, shared entanglement prepared ahead of time eliminates the need for a direct physical connection.

For trapped-ion systems, there are several proposals for scaling up to larger numbers of qubits. These include the “quantum charge-coupled device” (QCCD) architecture, which incorporates a large array of segmented trap electrodes to create different trapping zones designed for specialized roles such as loading ions, processing, and memory storage (4, 5). Qubits from different zones interact by being physically moved to the same zone. A variant of this approach couples different trapping zones by first creating entanglement between zones via a photonic network, followed by teleporting qubits (6). However, both approaches will benefit from a way

to perform gate operations between separated qubits via gate teleportation. Gate teleportation mitigates latency from transmitting quantum information between separated zones, provided that the required entangled ancilla pairs can be prepared and distributed ahead of time and concurrently with other unrelated processor functions.

Progress towards such distributed quantum computation has been made with quantum *state* teleportation, where an arbitrary state can be transferred between remote parties (1, 7); this has further applications in quantum repeaters (8) and quantum networks (9–11). Teleportation of quantum states has been demonstrated in various qubit platforms, including photons (12, 13), nuclear spins (14), trapped ions (15–17), atomic ensembles (18), superconducting circuits (19), and nitrogen-vacancy centers in diamond (20). A recent experiment teleported a photon polarization state between the ground and a satellite, demonstrating the potential for building large-scale quantum networks with this technique (21).

Using state teleportation, a universal two-qubit gate between two distant parties, Alice and Bob, can be implemented by teleporting Alice’s input state to Bob, applying local two-qubit gates at Bob’s location, and teleporting Alice’s half of the output back to her. This process consumes a minimum of two shared entangled pairs. For a CNOT gate, the same task can be achieved more efficiently using the protocol proposed by Eisert et al. (3) and depicted in Fig. 1a, without the need to physically bring the two qubits together or teleport the states back and forth. The Eisert protocol achieves the minimum possible overhead, requiring only a single entangled pair shared between the two distant locations, local operations, and classical communication.

This type of teleported entangling gate has been demonstrated probabilistically with photonic systems, where the required conditional operations were implemented with passive optical elements and post-selection (22, 23). More recently, a deterministic teleported CNOT gate was performed between two superconducting cavity qubits by means of an entangled pair of transmon qubits (24).

In this work, we demonstrate a deterministic teleported CNOT gate between two ${}^9\text{Be}^+$ ions through the use of a shared entangled pair of ${}^{25}\text{Mg}^+$ ions (Fig. 1b). Our experiment is the first trapped-ion implementation of gate teleportation, and it combines many key elements for scalable quantum computation on this platform, including separation and transport of mixed-species ion crystals, local two-qubit gates between the same and mixed species (25), individually-addressed single-qubit rotations and detection, and conditional operations based on the results of measurements on the entangled ancilla qubits (${}^{25}\text{Mg}^+$ in this experiment). The teleported CNOT gate operates on two qubits separated by more than $340\text{ }\mu\text{m}$ during the entire process. We use full process tomography to characterize the teleported CNOT gate.

The experiment is performed in a segmented linear Paul trap with two ${}^9\text{Be}^+$ and two ${}^{25}\text{Mg}^+$ ions. The qubits are encoded in the $|F=1, m_F=1\rangle_{\text{B}} \equiv |\uparrow\rangle_{\text{B}}$ and $|2, 0\rangle \equiv |\downarrow\rangle_{\text{B}}$ hyperfine states of ${}^9\text{Be}^+$ and the $|2, 0\rangle_{\text{M}} \equiv |\uparrow\rangle_{\text{M}}$ and $|3, 1\rangle_{\text{M}} \equiv |\downarrow\rangle_{\text{M}}$ states of ${}^{25}\text{Mg}^+$ ions. We use the symbol B (M) for ${}^9\text{Be}^+$ (${}^{25}\text{Mg}^+$) ions, and label all states of ${}^9\text{Be}^+$ (${}^{25}\text{Mg}^+$) ions with the subscript B (M) for the remainder of the manuscript. We label the two B ions as B_1, B_2 and the two M ions as M_1, M_2 . At the beginning of each experiment, a four-ion chain is initialized in the order $\text{B}_1\text{--}\text{M}_1\text{--}\text{M}_2\text{--}\text{B}_2$ in a potential well located where all laser beams pass through the trap, a region referred to as the laser interaction zone (LIZ) (Fig. 2). The internal state of a B (M) ion is determined by state-dependent fluorescence detection with resonant light at a wavelength of 313 nm (280 nm) after transferring the population from the computational basis to the measurement basis $|\uparrow\rangle_{\text{B}} \rightarrow |2, 2\rangle_{\text{B}} \equiv |\text{Bright}\rangle_{\text{B}}$ and $|\downarrow\rangle_{\text{B}} \rightarrow |1, -1\rangle_{\text{B}} \equiv |\text{Dark}\rangle_{\text{B}}$ ($|\downarrow\rangle_{\text{M}} \rightarrow |3, 3\rangle_{\text{M}} \equiv |\text{Bright}\rangle_{\text{M}}$ and $|\uparrow\rangle_{\text{M}} \rightarrow |2, -2\rangle_{\text{M}} \equiv |\text{Dark}\rangle_{\text{M}}$). See section Trap and Qubit in Supplementary Materials (SM) for more details (26). The segmented trap electrodes enable us to use time-varying potentials to split the ion crystals into selected subsets and transport them into and out of the LIZ (27, 28). This spatial separation enables individual addressing of ions of the same species, while ions of different species are distinguished spectroscopically due to their

well-separated resonant wavelengths.

We use stimulated Raman transitions for all coherent qubit operations on B and M ions. A pair of co-propagating laser beams for each species is used to drive single-qubit rotations where θ is the angle rotated and ϕ is the angle between the rotation axis (in the xy plane) and the positive x -axis of the Bloch sphere. A rotation around the z -axis $\hat{R}_Z(\alpha)$ is implemented by phase-shifting all subsequent single-qubit rotations for that qubit by $-\alpha$ (4). For definitions of the rotation matrices, see section Entangling Gates in SM (26). Each species uses a pair of perpendicular laser beams (each at 45 degrees with respect to the trap axis) to drive two-qubit Mølmer-Sørensen (MS) entangling gates for this species (29). Both pairs of Raman beams are applied simultaneously to drive mixed-species MS gates (25). We construct the $\text{CNOT}_{X \rightarrow Y}$ gate (where X is the control and Y is the target) and the Bell-state-generating gate \hat{F} using single-qubit rotations and MS gates (25, 30). For more details on the implementation, see section Entangling Gates in SM (26).

The circuit diagram for our implementation of a teleported CNOT is shown in Fig. 1c, and ion configurations and operations during gate teleportation are illustrated in Fig. 2. After sideband cooling (SBC) the four-ion chain by addressing the B ions, the algorithm begins with the B ions in the $|\text{Bright}\rangle_{\text{B}}$ state and the M ions in the $|\downarrow\rangle_{\text{M}}$ state. The gate \hat{F} is applied to the two M ions to generate the Bell state $|\Phi^-\rangle_{\text{M}} = \frac{1}{\sqrt{2}}(|\uparrow\uparrow\rangle_{\text{M}} - |\downarrow\downarrow\rangle_{\text{M}})$ (Fig. 2a). Afterwards, the four-ion chain is split into two B and M pairs residing in separated regions of a double-well potential (Fig. 2b), and we then translate the confining potential to bring the $\text{B}_1\text{--M}_1$ pair into the LIZ. There we ground-state cool the $\text{B}_1\text{--M}_1$ pair by addressing B_1 , prepare it to its input state, and apply $\text{CNOT}_{\text{B}_1 \rightarrow \text{M}_1}$. After this first CNOT gate, M_1 is mapped to the measurement basis and detected (Fig. 2c). The number of detected photons is compared to a preset threshold to determine the qubit state of M_1 . As described below, this information is later used to apply a conditional operation on M_2 . After this detection, the double well potential is translated so that

the M_2 – B_2 pair is moved into the LIZ, where it is ground-state cooled by addressing B_2 . The B_2 qubit is then prepared in its input state, and the conditional operation $\hat{R}(\pi, 0)$ is applied on M_2 only if M_1 was measured to be in the $|\downarrow\rangle_M$ state. Next we apply $\text{CNOT}_{M_2 \rightarrow B_2}$. The M_2 qubit is then mapped to the measurement basis and detected. A pulse selecting the measurement axis for state tomography is applied to B_2 , which is then mapped to the measurement basis, but not yet detected (Fig. 2d). This mapping reduces the depumping of B_2 from stray scattered light when detecting B_1 later in the process. The double well potential is then translated back to bring B_1 – M_1 into the LIZ, where we apply the conditional operation $\hat{R}_Z(\pi)$ only if M_2 was measured to be in the $|\downarrow\rangle_M$ state, followed by a single-qubit rotation selecting the measurement axis and a measurement of the state of B_1 (Fig. 2e). Subsequently, the ions are again shuttled to bring M_2 – B_2 into the LIZ where B_2 is detected (Fig. 2f). At the end of this sequence, the four-ion chain is recombined into the single well used at the beginning of the experiment to prepare it for the next repetition of the experiment (Fig. 2g).

To characterize our teleported CNOT gate between the two B ions, we used quantum process tomography (31). For the required informationally-complete set of measurements, the two B ions were prepared with single-qubit rotations in the following 16 different combinations of input states after initial state preparation to the $|\uparrow\uparrow\rangle_B$ state:

$$\begin{array}{cccc}
|\uparrow\uparrow\rangle_B & |\uparrow\downarrow\rangle_B & |\uparrow+\rangle_B & |\uparrow r\rangle_B \\
|\downarrow\uparrow\rangle_B & |\downarrow\downarrow\rangle_B & |\downarrow+\rangle_B & |\downarrow r\rangle_B \\
|+\uparrow\rangle_B & |+\downarrow\rangle_B & |++\rangle_B & |++r\rangle_B \\
|r\uparrow\rangle_B & |r\downarrow\rangle_B & |r+\rangle_B & |rr\rangle_B
\end{array}$$

where $|+\rangle_B = \frac{1}{\sqrt{2}}(|\uparrow\rangle_B + |\downarrow\rangle_B)$ and $|r\rangle_B = \frac{1}{\sqrt{2}}(|\uparrow\rangle_B + i|\downarrow\rangle_B)$. For each of these 16 inputs, the output states were then measured along the 9 different combinations of measurement axes $XX, XY, XZ, YX, YY, YZ, ZX, ZY, ZZ$, where a measurement along the Z axis was implemented by transferring to the measurement basis and performing fluorescence detection, and a measurement along the X or Y axis was performed similarly after a rotation $\hat{R}(\pi/2, -\pi/2)$

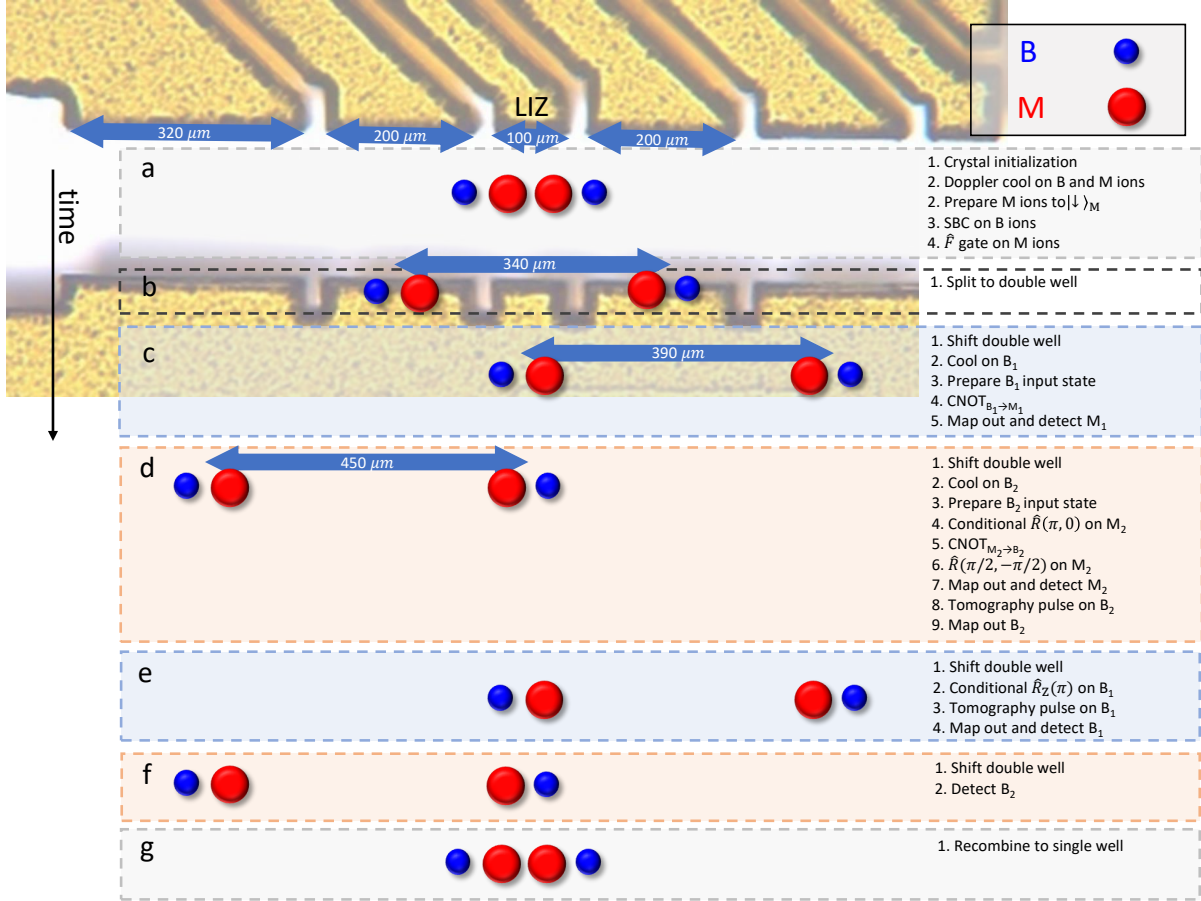


Figure 2: Gate teleportation implementation with shuttling sequence. Panels a-g show the algorithm and the shuttling sequence, overlaid on a photograph of a section of the trap electrode structure (ion spacings are not to scale). After preparing the M ions in a Bell state to serve as the entanglement resource, the four-ion chain B–M–M–B is split into two pairs of B and M ions, which are translated into and out of the laser interaction zone (LIZ) to address and detect individual ions (blocks c, d, e and f). The detection results from the two M ions at step (c5) and (d7) are used as inputs to trigger the required conditional operations. The blue arrows indicate the dimensions of the trap and the spacing between the two potential wells.

or $\hat{R}(\pi/2, 0)$, respectively. The 144 different combinations of input states and measurement axes were implemented in random order, with approximately 300 consecutive executions of the experiment for each combination.

Two complete sets of tomography data were acquired. We developed a protocol for data

analysis on Data Set 1 while remaining blind to Data Set 2, and then applied this protocol to Data Set 2. We summarize the analysis methods and results for Data Set 2 below.

From the observed measurement outcomes, we determined the most likely quantum process by maximum likelihood (ML) estimation, and inferred a 95% confidence interval of $[0.845, 0.872]$ for the entanglement fidelity with respect to an ideal CNOT. The matrix representing the quantum process is shown in Fig. 3. As a consistency check against the ML fidelity estimate, we also constructed an estimator to compute the fidelity as a linear combination of the observed probabilities. From this method, we obtained a 95% confidence interval of $[0.845, 0.888]$ for the entanglement fidelity. Since the ML method provides less uncertainty than the linear estimator, we focus our report on the confidence interval constructed by ML. For details of our analysis, see section Quantum Process Tomography in SM (26).

Ideally, the observed data should be consistent with the assumption of a single quantum process, but fluctuations and uncontrolled drifts in control parameters on time-scales much slower than a single gate-teleportation process will lead to imperfections. To detect departure from this assumption and to discover unchecked fluctuations, we applied a likelihood ratio test (32), similar to that described in (33). For a full description of all assumptions and the likelihood ratio test, see section Quantum Process Tomography in SM (26). A likelihood ratio was computed from the experimental data and compared to the distribution of likelihood ratios obtained from synthetic datasets generated by parametric bootstrapping (34). The test indicated that our data was inconsistent with a single quantum process. Motivated by this finding, we discovered drifts in the single-qubit-rotation angles applied to B_1 and B_2 that eluded our direct feedback on laser beam power and were not sufficiently reduced by the sparse calibration of pulse durations during data acquisition. We verified through numerical simulation that fluctuations of single-qubit-rotation angles over several hours and with the approximate magnitude as diagnosed in the experimental setup affect state preparation, tomography, and construction of entangling gates,

resulting in an inconsistency comparable to what we observed in our data. This suggests that such consistency checks are an important diagnostic that can supplement other benchmarking techniques and uncover sources of infidelity that would otherwise remain unchecked.

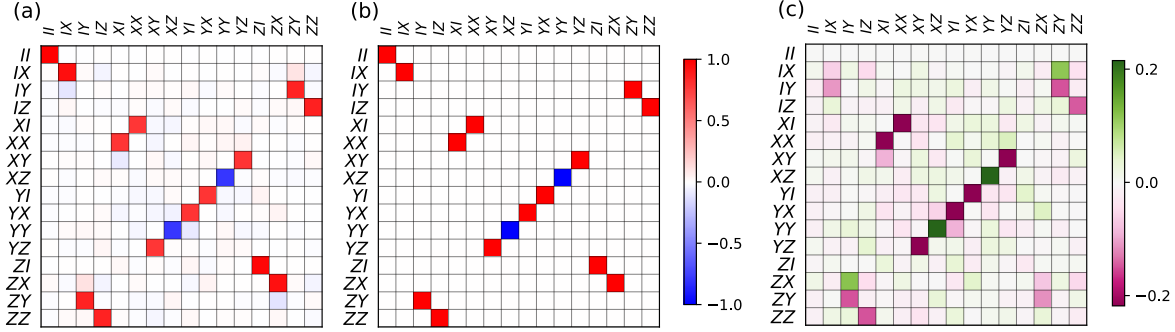


Figure 3: **Pauli transfer matrix.** Visualization of quantum processes in the Pauli transfer matrix representation for (a) the experimental data “Data Set 2”, (b) the ideal CNOT process, and (c) the difference of the experimental and the ideal process matrices (experimental data minus ideal data). The entries of the Pauli transfer matrix from experimental data are real numbers between -1 and $+1$ with their values indicated by the colorbar. The ideal process matrix is restricted to entries with values -1 , 0 , and 1 . For the definition of the representation, see section Pauli Transfer Matrix in SM (26).

In addition to performing the likelihood ratio test, we also studied the influence of known sources of decoherence and control errors on the process fidelity in our gate teleportation demonstration. We considered error sources in the following elements of our experiment: state preparation and measurement (SPAM) of the B and M ions, the creation of the M_1 – M_2 Bell state (excluding SPAM), the two CNOT gates, and the decoherence of the M ions, with the corresponding error values listed in Table 1. The decoherence of the B ions contributes much less significantly because of its long coherence time. See section Trap and Qubit in SM for more details (26). In addition to these errors, we observe that resonant stray light causes depumping errors in ions located away from the LIZ. Specifically, the detection pulse on M_1 induces a depumping error on M_2 of $0.011(4)$ and the repumping pulses during SBC with B_2 induce a similar error on B_1 of $0.012(3)$. See section Error Sources in SM for more details (26).

Table 1: **Error sources for the teleported CNOT gate.** The Bell state fidelity with the contribution of the SPAM errors subtracted is used as an estimate of the mixed-species CNOT gate fidelity. The error bars correspond to 1σ -uncertainty for the respective error sources. See section Error Sources in SM for more details.

Sources	Error (10^{-2})
SPAM on two B ions	1.1(7)
SPAM on two M ions	1.5(3)
M ₁ -M ₂ Bell state	4.0(9)
B ₁ -M ₁ CNOT	3.0(9)
M ₂ -B ₂ CNOT	3(1)
Coherence of M ions	0.7(3)
Stray light from M ₁ detection on M ₂	1.1(4)
Stray light from B ₂ cooling on B ₁	1.2(3)
Sum	16(2)
Depolarizing model	12(1)

Treating all errors as mutually independent, the total error is approximately given by their sum, while the uncertainties add in quadrature. The total error equals 0.16(2). To obtain a more accurate description of the impact of the individual errors on the total process fidelity, we formulate the contribution from individual processes with a depolarizing model

$$\rho \rightarrow (1 - \epsilon)\hat{U}\rho\hat{U}^\dagger + \epsilon \cdot \hat{I}/d, \quad (1)$$

where ϵ is the error of the process \hat{U} , \hat{I} is the identity matrix, and d is the dimension of the Hilbert space for the process (35). Using experimentally determined errors for individual processes, the depolarizing model predicts a process fidelity of 0.88(1), which is near the upper limits of the 95% confidence intervals derived from our fidelity estimators, indicating that the major error sources are included in the error propagation model.

We now briefly discuss issues relating to scaling, alternative implementations, and future improvements. The gate teleportation algorithm we implemented uses a four-ion chain, where both B and M ions serve as qubit and coolant ions. Since cooling erases quantum information,

any quantum information encoded in the B ions prior to the start of the experiment gets destroyed. Our implementation therefore cannot be embedded in a larger quantum circuit. This can be avoided by adding extra ions exclusively for cooling.

In our experiment we produced the required entanglement with a unitary entangling gate on M ions; however this need not be the case. Alternative methods, such as dissipative entanglement (36) or Hilbert space engineering (37), could be used to generate Bell states as entanglement resources, potentially providing faster entangling rates or higher Bell state fidelity. Finally, there is the issue of our use of shuttling to achieve individual addressing of separated ion pairs. Ideally, we would implement the algorithm with the ions always positioned as in block b of Fig. 2, and direct laser beams at the individual wells. This is possible, but it would add complexity to optical arrangement of our demonstration experiment.

In summary, we demonstrated a deterministic teleported CNOT gate between two spatially separated beryllium ions, with an entanglement fidelity confidence interval of $[0.845, 0.872]$ at the 95% level. Such gates can serve as a useful primitive for large-scale quantum computation. For the first time, we integrated several operations into a single experiment, including mixed-species coherent control, ion transport, and entangling operations on selected subsets of the system. This will be essential for building large-scale quantum computers based on ions in the QCCD architecture (5). Moreover, applying consistency checks to the experimental data facilitated the identification of error sources in the experimental setup. This illustrates the importance of performing consistency checks in addition to tomography when characterizing quantum processes, and we expect this to be an important tool in future work.

References and Notes

1. D. Gottesman, I. L. Chuang, Demonstrating the viability of universal quantum computation using teleportation and single-qubit operations, *Nature* **402**, 390 (1999).

2. J. Preskill, Quantum Computing in the NISQ era and beyond, *Quantum* **2**, 79 (2018).
3. J. Eisert, K. Jacobs, P. Papadopoulos, M. B. Plenio, Optimal local implementation of non-local quantum gates, *Physical Review A* **62**, 052317 (2000).
4. D. J. Wineland, *et al.*, Experimental issues in coherent quantum-state manipulation of trapped atomic ions, *Journal of Research of the National Institute of Standards and Technology* **103**, 259 (1998).
5. D. Kielpinski, C. Monroe, D. J. Wineland, Architecture for a large-scale ion-trap quantum computer, *Nature* **417**, 709 (2002).
6. C. Monroe, *et al.*, Large-scale modular quantum-computer architecture with atomic memory and photonic interconnects, *Physical Review A* **89**, 022317 (2014).
7. C. H. Bennett, *et al.*, Teleporting an unknown quantum state via dual classical and Einstein-Podolsky-Rosen channels, *Physical Review Letters* **70**, 1895 (1993).
8. H.-J. Briegel, W. Dür, J. I. Cirac, P. Zoller, Quantum Repeaters: The Role of Imperfect Local Operations in Quantum Communication, *Physical Review Letters* **81**, 5932 (1998).
9. J. I. Cirac, P. Zoller, H. J. Kimble, H. Mabuchi, Quantum State Transfer and Entanglement Distribution among Distant Nodes in a Quantum Network, *Physical Review Letters* **78**, 3221 (1997).
10. P. van Loock, S. L. Braunstein, Multipartite Entanglement for Continuous Variables: A Quantum Teleportation Network, *Physical Review Letters* **84**, 3482 (2000).
11. H. Yonezawa, T. Aoki, A. Furusawa, Demonstration of a quantum teleportation network for continuous variables, *Nature* **431**, 430 (2004).

12. D. Bouwmeester, *et al.*, Experimental quantum teleportation, *Nature* **390**, 575 (1997).
13. D. Boschi, S. Branca, F. De Martini, L. Hardy, S. Popescu, Experimental Realization of Teleporting an Unknown Pure Quantum State via Dual Classical and Einstein-Podolsky-Rosen Channels, *Physical Review Letters* **80**, 1121 (1998).
14. M. A. Nielsen, E. Knill, R. Laflamme, Complete quantum teleportation using nuclear magnetic resonance, *Nature* **396**, 52 (1998).
15. M. Riebe, *et al.*, Deterministic quantum teleportation with atoms, *Nature* **429**, 734 (2004).
16. M. D. Barrett, *et al.*, Deterministic quantum teleportation of atomic qubits, *Nature* **429**, 737 (2004).
17. S. Olmschenk, *et al.*, Quantum Teleportation Between Distant Matter Qubits, *Science* **323**, 486 (2009).
18. X.-H. Bao, *et al.*, Quantum teleportation between remote atomic-ensemble quantum memories, *Proceedings of the National Academy of Sciences* **109**, 20347 (2012).
19. L. Steffen, *et al.*, Deterministic quantum teleportation with feed-forward in a solid state system, *Nature* **500**, 319 (2013).
20. W. Pfaff, *et al.*, Unconditional quantum teleportation between distant solid-state quantum bits, *Science* **345**, 532 (2014).
21. J.-G. Ren, *et al.*, Ground-to-satellite quantum teleportation, *Nature* **549**, 70 (2017).
22. Y.-F. Huang, X.-F. Ren, Y.-S. Zhang, L.-M. Duan, G.-C. Guo, Experimental Teleportation of a Quantum Controlled-NOT Gate, *Physical Review Letters* **93**, 240501 (2004).

23. W.-B. Gao, *et al.*, Teleportation-based realization of an optical quantum two-qubit entangling gate, *Proceedings of the National Academy of Sciences* **107**, 20869 (2010).
24. K. S. Chou, *et al.*, Deterministic teleportation of a quantum gate between two logical qubits, *Nature* **561**, 368 (2018).
25. T. R. Tan, *et al.*, Multi-element logic gates for trapped-ion qubits, *Nature* **528**, 380 (2015).
26. Materials and methods are available as supplementary materials on Science Online.
27. R. B. Blakestad, *et al.*, High-fidelity transport of trapped-ion qubits through an X-junction trap array, *Phys. Rev. Lett.* **102**, 153002 (2009).
28. R. B. Blakestad, *et al.*, Near-ground-state transport of trapped-ion qubits through a multi-dimensional array, *Physical Review A* **84**, 032314 (2011).
29. A. Sørensen, K. Mølmer, Quantum computation with ions in thermal motion, *Phys. Rev. Lett.* **82**, 1971 (1999).
30. P. J. Lee, *et al.*, Phase control of trapped ion quantum gates, *Journal of Optics B: Quantum and Semiclassical Optics* **7**, S371 (2005).
31. I. L. Chuang, M. A. Nielsen, Prescription for experimental determination of the dynamics of a quantum black box, *Journal of Modern Optics* **44**, 2455 (1997).
32. G. Casella, R. L. Berger, *Statistical Inference* (Cengage Learning, 2001), p. 374.
33. R. Blume-Kohout, *et al.*, Demonstration of qubit operations below a rigorous fault tolerance threshold with gate set tomography, *Nature Communications* **8**, 14485 (2017).
34. B. Efron, R. J. Tibshirani, *An Introduction to the Bootstrap* (CRC Press, 1994).

35. E. Knill, *et al.*, Introduction to Quantum Error Correction, *arXiv:quant-ph/0207170* (2002).
36. Y. Lin, *et al.*, Dissipative production of a maximally entangled steady state of two quantum bits, *Nature* **504**, 415 (2013).
37. Y. Lin, *et al.*, Preparation of Entangled States through Hilbert Space Engineering, *Physical Review Letters* **117**, 140502 (2016).

Acknowledgments

We thank P. Hou and D. Cole of NIST ion storage group for comments on the manuscript. We thank D. T. C. Allcock, S. C. Burd (both of the NIST ion storage group), the Oxford University, and the ETH Zürich ion trapping groups for their advice on stabilizing magnetic fields. This work was supported by the Office of the Director of National Intelligence (ODNI) Intelligence Advanced Research Projects Activity (IARPA), ONR, and the NIST Quantum Information Program. D.K. acknowledges support from the Swiss National Science Foundation under grant no. 165208. S.D.E. acknowledges support by the U.S. National Science Foundation under Grant No. DGE 1650115. Y.W., D.K., J.J.W., and H.M.V. are associates in the Professional Research Experience Program (PREP) operated jointly by NIST and University of Colorado Boulder, and acknowledge this support. H.M.V. acknowledges support from the Schlumberger Foundation’s Faculty for the Future program.

List of Supplementary Materials

Supplementary Text

Table S1–S3

Figure S1–S9

References (38–47)

Supplementary Materials

Trap and Qubit This experiment is performed in a multi-layer segmented linear Paul trap, described in detail in (28). We use ${}^9\text{Be}^+$ and ${}^{25}\text{Mg}^+$ as qubits at a magnetic field of 1.19×10^{-2} T. The detailed level structures for both qubits are depicted in Fig. S1. The qubits are encoded in the Zeeman sublevels of the hyperfine groundstate manifolds $|1, 1\rangle_{\text{B}} \equiv |\uparrow\rangle_{\text{B}}$ and $|2, 0\rangle_{\text{B}} \equiv |\downarrow\rangle_{\text{B}}$ for ${}^9\text{Be}^+$ ions and $|2, 0\rangle_{\text{M}} \equiv |\uparrow\rangle_{\text{M}}$ and $|3, 1\rangle_{\text{M}} \equiv |\downarrow\rangle_{\text{M}}$ for ${}^{25}\text{Mg}^+$ ions. As in the main text, we use the symbol B (M) for ${}^9\text{Be}^+$ (${}^{25}\text{Mg}^+$) ions, and label all states of ${}^9\text{Be}^+$ (${}^{25}\text{Mg}^+$) ions with the subscript B (M) for the remainder of the manuscript. At our chosen magnetic field (1.19×10^{-2} T), the B qubits are first-order insensitive to magnetic field fluctuations. A Ramsey experiment with microwave pulses shows contrast higher than 90% after a Ramsey wait time of 1 s; a Ramsey experiment with co-propagating laser carrier pulses shows similar results. The M qubits are first-order sensitive to magnetic field fluctuations with a linear coefficient of $\sim 430 \text{ kHz mT}^{-1}$ (25). We stabilize the magnetic field by measuring the current applied to the magnetic field coils and feeding back on the voltage setpoint of the current supply to keep the measured current stable. Individual components of the algorithm are generally calibrated in experiments triggered on the 60 Hz AC line, but they typically occur at different phases of the cycle than their use in the gate teleportation algorithm. To mitigate miscalibrations from this, we modulate the magnetic field current feedback setpoint with 60 Hz and 180 Hz signals (phases relative to the AC cycle and amplitudes determined experimentally) to reduce the magnetic field noise amplitude at these frequencies. We additionally synchronize the gate teleportation algorithm with the 60 Hz AC line cycle to reduce decoherence caused by the remaining magnetic field noise at 60 Hz and its harmonics. These improvements result in a coherence time of ~ 140 ms on the M qubit transition, measured independently in a Ramsey experiment using microwave pulses and in another Ramsey experiment using co-propagating

Raman beams. Slow fluctuations in the ambient magnetic field noise lead to variations of the coherence time by up to 30% from day to day.

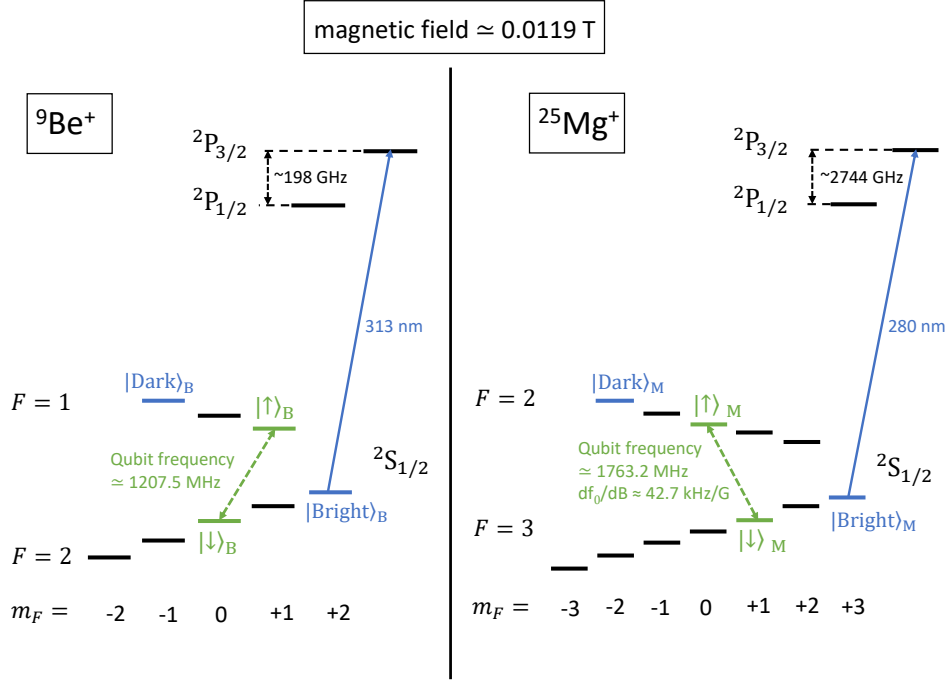


Figure S1: **Relevant level structures of beryllium and magnesium ions.** The $^9\text{Be}^+$ qubits are encoded in the computation basis $|\uparrow\rangle_B$ and $|\downarrow\rangle_B$ and mapped out to the measurement basis $|\text{Bright}\rangle_B$ and $|\text{Dark}\rangle_B$ respectively for fluorescence detection with 313 nm light. The $^{25}\text{Mg}^+$ qubits are encoded in the computation basis $|\uparrow\rangle_M$ and $|\downarrow\rangle_M$ and mapped out to the measurement basis $|\text{Dark}\rangle_M$ and $|\text{Bright}\rangle_M$ respectively for fluorescence detection with 280 nm light. (See text)

All laser beams used in this experiment are aligned to the ions at the laser interaction zone (LIZ). At this location in the trap, both B and M ions experience axial micromotion (due to trap imperfections), with a modulation index of 2.67 for B ions and 1.08 for M ions (27). An electro-optic modulator (EOM) is placed in one of the B motion-sensitive Raman beamlines to compensate for this effect and results in an effective modulation index of less than 0.1 for B; M axial micromotion is left uncompensated. All B motion-sensitive Raman transitions in this work are driven on the micromotion carrier instead of the second micromotion sideband as done

in previous work in this trap (25, 38).

Crystal Preparation Prior to running experiments, we load a four-ion chain of two B ions and two M ions into a single well located at the LIZ with trap frequencies of 2.0 MHz axial, 12.0 MHz and 12.3 MHz radial for a single B ion.

The initial order of ions in the ion crystal is random and can change on the time-scales of minutes from background gas collisions. To set the order before each shot of the experiment, we increase the axial potential (trap frequencies of 5.5 MHz axial, 10.5 MHz and 12.5 MHz radial for a single B ion) while simultaneously laser cooling both species. In this case, the four-ion chain is deformed into an energetically favorable diamond-shaped configuration where the two M ions are aligned radially and displaced symmetrically about the z -axis between the two B ions. Relaxing the trap back to the original confining potential brings the crystal to an ordered linear chain of B–M–M–B, with trap frequencies of 1.4 MHz, 3.0 MHz, 4.1 MHz, and 4.2 MHz for the four different axial modes. As in the main text, we label the four qubits sequentially as B_1, M_1, M_2, B_2 .

Shuttling Operations To individually address the two pairs of B and M ions, the four-ion chain is separated into B_1 – M_1 and M_2 – B_2 in a process taking $570 \mu\text{s}$ (Fig. 2a \rightarrow 2b). The two ion pairs can then be individually shuttled to the LIZ by applying shuttling steps from a set of four primitives, each taking $230 \mu\text{s}$. This set includes shuttling from the ion positions shown in Fig. 2b \rightarrow 2c, 2b \rightarrow 2d, and their time reversals. The full shuttling sequence is concatenated from these basic separation and transport operations (27, 28). While residing in the LIZ, the pairs of B and M ions are confined in a potential with axial trap frequencies of 2.1 MHz and 4.5 MHz.

State Preparation and Detection To prepare for each experiment, the B and M ions are optically pumped to $|\text{Bright}\rangle_{\text{B}}$ for B and $|\text{Bright}\rangle_{\text{M}}$ for M. The M ions are then transferred to the state $|\downarrow\rangle_{\text{M}}$ with microwave pulses. To detect their internal states, the ions are mapped from the computation basis to the measurement basis. The B ions are mapped individually with co-propagating Raman beams from $|\uparrow\rangle_{\text{B}}$ to $|\text{Bright}\rangle_{\text{B}}$ and from $|\downarrow\rangle_{\text{B}}$ to $|\text{Dark}\rangle_{\text{B}}$, while the M ions are mapped with a combined scheme

$$|\downarrow\rangle_{\text{M}} \xrightarrow{\text{laser}} |2, +2\rangle_{\text{M}} \xrightarrow{\text{microwave}} |\text{Bright}\rangle_{\text{M}} \quad (2)$$

$$|\uparrow\rangle_{\text{M}} \xrightarrow{\text{laser}} |3, -1\rangle_{\text{M}} \xrightarrow{\text{microwave}} |\text{Dark}\rangle_{\text{M}} \quad (3)$$

to maintain both individual addressing and high transfer efficiency¹. After mapping out to the measurement basis, the internal states of the ions are distinguished by fluorescence detection for a duration of $330 \mu\text{s}$ for B and $200 \mu\text{s}$ for M ions. An EOM is placed in the B resonant beamline to approximately cancel the effect of axial micromotion. We obtain an approximately Poissonian distribution of photon counts with a mean of roughly 30 counts for each individual B and M ion in the bright state, and average background counts of 1.5 and 0.8 for B and M respectively in the dark state. For conditional operations based on the M measurements, a threshold of 10 photon counts is set to distinguish $|\text{Bright}\rangle_{\text{M}}$ from $|\text{Dark}\rangle_{\text{M}}$ in a single measurement. Thresholds for the B measurements are discussed in the quantum process tomography section below.

Sideband Cooling At the beginning of the algorithm, we apply Doppler cooling (DC) on both M and B ions followed by sideband cooling (SBC) on the B ions (39). The SBC sequence consists of continuous SBC applied sequentially to the four axial modes (40) followed by a short sequence of pulsed SBC (39), which cools the four-ion chain to an average motional quantum number \bar{n} of less than 0.1 for the mode used to implement the MS gate and less than 0.3 for all

¹In contrast, all qubit operations for both species are implemented with laser pulses.

the other axial modes. After separating the two B and M pairs and shuttling one pair of B and M ions to the LIZ (Fig 2c and 2d), Doppler cooling is only applied to the B ions to preserve the entanglement of the M qubits. SBC on B ions cools the axial modes of the B and M pairs to an average occupation number \bar{n} of less than 0.1 before applying two-qubit gate operations.

Entangling Gates Two sets of Raman laser beams are used to implement the single-qubit and two-qubit operations in this experiment. For the M ions, a frequency-quadrupled diode laser (~ 295 GHz blue-detuned from the $S_{1/2} \leftrightarrow P_{3/2}$ transition) is used to produce all the frequencies necessary for driving co-propagating carrier transitions, motion-sensitive carrier transitions, and two-qubit Mølmer-Sørensen (MS) gates. Similarly, all laser beams for addressing the B ions are derived from a fiber laser system (~ 265 GHz red-detuned from the $S_{1/2} \leftrightarrow P_{1/2}$ transition). The co-propagating carrier pulses induce single-qubit rotations

$$\hat{R}(\theta, \phi) = \begin{bmatrix} \cos \frac{\theta}{2} & -ie^{-i\phi} \sin \frac{\theta}{2} \\ -ie^{i\phi} \sin \frac{\theta}{2} & \cos \frac{\theta}{2} \end{bmatrix} \quad (4)$$

where θ is the angle rotated and ϕ is the angle between the rotation axis (in the xy plane) and the positive x -axis of the Bloch sphere.

We use a pair of M ions in the Bell state $|\Phi^-\rangle_M = \frac{1}{\sqrt{2}}(|\uparrow\uparrow\rangle_M - |\downarrow\downarrow\rangle_M)$ as the entanglement resource for the teleported CNOT gate. This entangled pair is generated with a MS interaction applied only to the M ions in the four-ion chain. The gate is implemented on the out-of-phase mode at 3.0 MHz with a gate duration of about $56 \mu\text{s}$. The MS interaction implemented here does not generate a deterministic Bell state due to a fluctuating interferometric phase between the two arms of the motion sensitive Raman beams. To mitigate this, the MS pulse is surrounded with a pair of motion-sensitive carrier $\pi/2$ pulses, resulting in the phase gate we call \hat{G} as shown in Fig. S2a (30). Further surrounding \hat{G} with a pair of co-propagating carrier $\pi/2$ pulses constructs the Bell-state-generating gate \hat{F} used to entangle the two M ions (Fig. S2b).

The entangling gates within the B and M pairs are implemented by a mixed-species MS

interaction on the in-phase mode at 2.1 MHz (25). We produce \hat{G} as discussed for the single species gate above and apply additional co-propagating carrier $\pi/2$ pulses on the M (B) ion to construct the $\text{CNOT}_{B_1 \rightarrow M_1}$ ($\text{CNOT}_{M_2 \rightarrow B_2}$) operation with B (M) as the control (Fig. S2c). The rotation

$$\hat{R}_Z(\alpha) = \begin{bmatrix} e^{-i\alpha/2} & 0 \\ 0 & e^{i\alpha/2} \end{bmatrix} \quad (5)$$

at the end of the pulse group is implemented in software by changing the phase of subsequent single-qubit rotations for that qubit by $-\alpha$. This requires that two-qubit gates commute with $\hat{R}_Z(\alpha)$ rotations, and this requirement is fulfilled for the phase gate \hat{G} .

Phase Tracking The experiment is performed with a direct digital synthesizer (DDS) running in the “absolute phase” mode, where the phase of the DDS is reset if a frequency or phase change is necessary. The phase evolution of the qubits in the laboratory frame is tracked on the experiment control computer by accounting for the free precession frequency f_0 of the qubits and the precise timing t from the first pulse to the current pulse. To apply a rotation at phase ϕ , the corresponding DDS is set to the phase $2\pi \cdot f_0 \cdot t + \phi + \phi_0$, where the additional offset ϕ_0 takes into account the phase shifts induced by the AC-Stark effect and magnetic field gradient. This removes the requirement of tracking the phase of each individual qubit with an independent DDS. In this experiment, we calibrate the phase offset ϕ_0 for each co-propagating carrier pulse with a separate Ramsey experiment. This could be avoided in future experiments by calibrating the AC-Stark shift and the magnetic-field-gradient-induced phase shift and calculating the required phases from these calibrations.

Drifts and Calibration To improve the long-term stability of our experiment, parameters such as pulse lengths and transition frequencies are re-calibrated during data acquisition to reduce the effect of slow drifts in laser output, beam pointing, and magnetic field strength. We

Table S1: **Detailed steps of the gate teleportation algorithm with the approximate durations of each step.** The majority of the time is spent on cooling and shuttling the ions. DC: Doppler cooling, SP: state preparation, SBC: sideband cooling. The additional M ion detections in steps e and f are for diagnostics and are not part of the gate teleportation algorithm.

Step	Description	Operation	Duration
	Optical pumping and crystal initialization of the four-ion chain	-	3.2 ms
a	DC on B and M and SP of M ions	-	1.3 ms
	SBC on B ions	-	5.3 ms
	M_1 – M_2 Bell state generation	\hat{F}	220 μ s
b	Separation of four-ion chain into B_1 – M_1 and M_2 – B_2 in double well	-	570 μ s
	Shifting double well	-	230 μ s
c	DC, SBC, and SP of B_1	-	2.2 ms
	CNOT on B_1 – M_1	CNOT	280 μ s
	Map out and detection of M_1	-	650 μ s
	Shifting double well	-	460 μ s
	Cooling and SP of B_2	-	2.2 ms
d	Conditional rotation on M_2	$\hat{R}(\pi, 0)$	25 μ s
	CNOT on B_2 – M_2	CNOT	280 μ s
	Rotation on M_2	$\hat{R}(\pi/2, -\pi/2)$	15 μ s
	Map out and detection of M_2	-	650 μ s
	Map out B_2	-	220 μ s
	Shifting double well	-	460 μ s
e	DC on M_1	-	200 μ s
	Conditional phase shift on B_1	$\hat{R}_Z(\pi)$	100 ns
	Map out and detection of B_1	-	540 μ s
	Detection of M_1	-	180 μ s
	Shifting double well	-	460 μ s
f	DC on M_2	-	200 μ s
	Detection of B_2	-	300 μ s
	Detection of M_2	-	180 μ s
g	Recombination	-	800 μ s

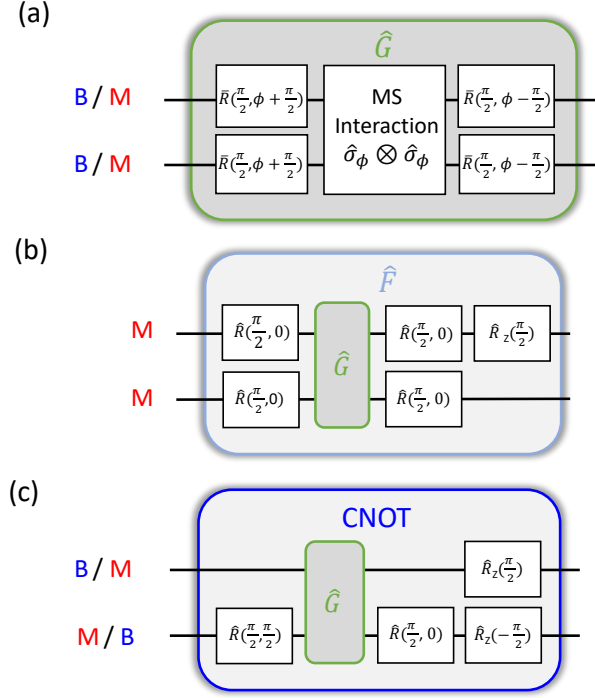


Figure S2: **Composite gates.** (a) The phase gate \hat{G} is constructed by surrounding the MS pulse with single-qubit rotations \bar{R} , both driven by motion-sensitive Raman beams. The notation \bar{R} distinguishes itself from motion-insensitive single-qubit rotations \hat{R} driven by co-propagating Raman beams. The resulting operation does not depend on the uncontrolled interferometric phase of the Raman beam sets. (b) The Bell-state-generating gate \hat{F} is constructed by surrounding \hat{G} with co-propagating $\pi/2$ pulses and phase-shifting one of the qubits by $\pi/2$ at the end. Starting from the $|\downarrow\downarrow\rangle_M$ state, the sequence generates a Bell state $|\Phi^-\rangle_M = \frac{1}{\sqrt{2}}(|\uparrow\uparrow\rangle_M - |\downarrow\downarrow\rangle_M)$. (c) The CNOT gate is constructed by surrounding \hat{G} with co-propagating $\pi/2$ pulses on the target qubit and phase shifting the control and the target qubit by $\pi/2$ and $-\pi/2$ respectively.

observe that these experimental parameters drift significantly over time-scales of several minutes to hours, which affects the fidelity of the algorithm and all its components. For example, Fig. S3 shows the measurements of the fidelity of the M_1 – M_2 Bell state (without correcting for SPAM) over a period of four hours without recalibration. After the initial calibration, the fidelity of the Bell state drifts away from the value obtained immediately after calibration. Therefore, to maintain all of the operations used in this experiment at a nearly constant and high fidelity, running the algorithm is conditioned upon fulfilling several validation experiments (validators).

The validators verify that parameters were sufficiently accurate within a predetermined time period before the algorithm is scheduled, otherwise re-calibration is triggered. Each validator is again conditioned on its dependencies. Taking the B co-propagating carrier rotation $\hat{R}(\pi/2, 0)$ as an example: With B ions initialized in $|\uparrow\rangle_B$, the carrier $\pi/2$ pulses are validated by observing that 1) the probability of four successive pulses bringing the ions back to $|\uparrow\rangle_B$ and 2) the probability of six successive pulses bringing the ions to $|\downarrow\rangle_B$ are both higher than their pre-defined thresholds. Failing the validation will trigger recalibration of the pulse parameters (pulse duration, transition frequency, and phase offset between subsequent pulses) and validators of the pulse parameters' dependencies. Here, the calibration of the pulse parameters of the B co-propagating carrier rotations relies on the correct values of magnetic field and mapping pulses, which serve as the dependencies.

Maintaining the fidelity of these operations at a consistent level significantly decreases systematic noise from experimental drifts. As shown in Fig. S4, we track the fidelities of Bell states generated from the MS, \hat{F} and CNOT gates while taking tomography data. The standard deviation of these measurements does not differ significantly from the uncertainty of the individual measurements due to projection noise.

Quantum Process Tomography We collected two full data sets for process tomography, and used Data Set 1 to develop the final analysis protocol to be applied blindly to Data Set 2. Process tomography is performed by preparing an informationally-complete set of input states $\{\rho_k\}_{k=1}^{16}$, applying the teleportation algorithm to each input state, and measuring the two B ions in one of the 9 possible Pauli-product bases. The set of input states is listed in the main text. Each measurement basis constitutes a positive operator-valued measure (POVM) with 4 elements, corresponding to the detections of bright or dark states of the two ions. The family of 4×9 POVM elements $\{E_l\}_{l=1}^{36}$ obtained from the POVMs for the 9 measurement bases is

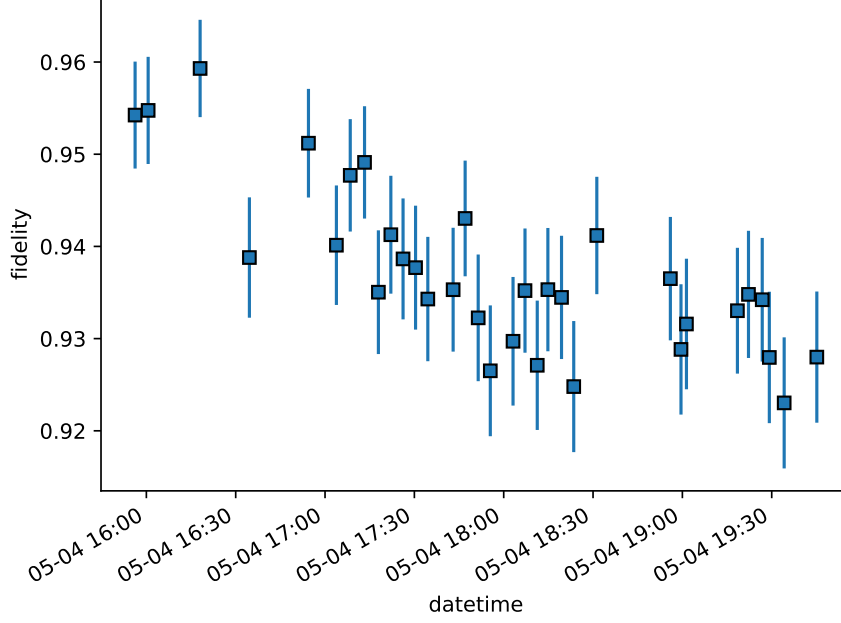


Figure S3: **Drifts of gate fidelity.** The fidelity of the M Bell state generated by \hat{F} is measured continuously over a period of four hours without re-calibration of experimental parameters, showing the drift away from the initial value over time. This drift behavior varies from run to run. The data is taken on May 04, 2018. The gaps near 16:00 and 18:30 are caused by reloading the ions.

informationally complete for state tomography. We refer to running the algorithm with a single choice of state preparation and measurement basis as an *experiment*, and a single instance of input state preparation, teleportation algorithm, and measurement as a *trial*. We assume perfect preparation of the input B states, but to account for the small overlap between photon-count distributions of the bright and dark states during detection, we model the POVM elements for individual ion measurements as a convex sum of projectors onto the bright and dark states. From a set of reference photon count histograms recorded periodically between experiments during the data acquisition, we infer the POVM elements by finding the thresholds and weights in the convex sum that maximize the likelihood of the observed reference histogram data (See

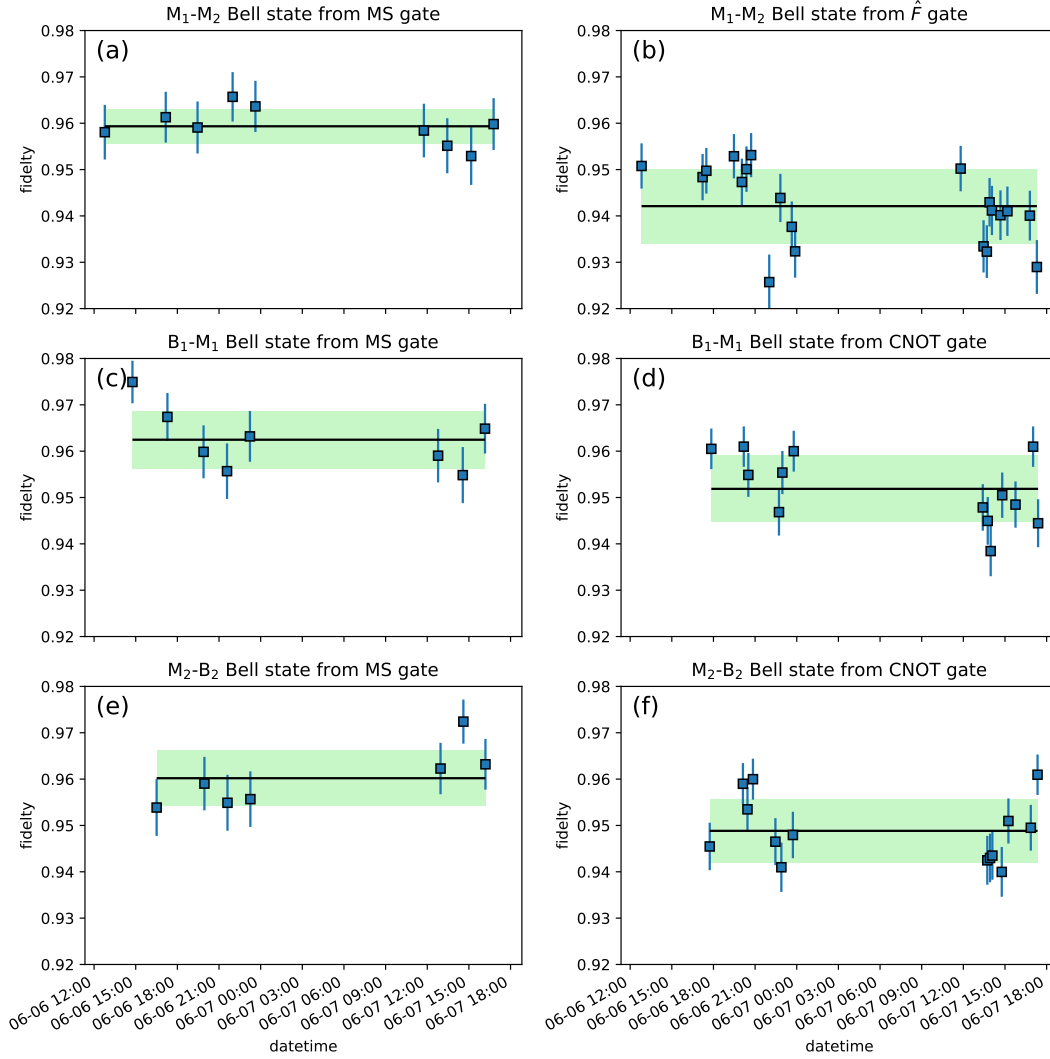


Figure S4: **Bell state fidelities.** Bell state fidelity measurements while taking full process tomography data on the teleported CNOT, without correcting for SPAM. The measurement spans over two days from June 6 to June 7, 2018. (a) M_1 - M_2 Bell state from the MS gate. (b) M_1 - M_2 Bell state from \hat{F} . For (a) and (b), microwave pulses are used for mapping into and out of the computation basis. (c) B_1 - M_1 Bell state from MS gate (d) B_1 - M_1 Bell state from CNOT gate (e) M_2 - B_2 Bell state from MS gate (f) M_2 - B_2 Bell state from CNOT gate. Squares: fidelity data. Solid black line: Mean fidelity. Green band: standard deviation of the data points. The error bars on the fidelity data are the uncertainties of each fidelity measurement due to projection noise.

Fig. S5).

Given a quantum process \mathcal{E} applied to input state ρ_k , the probability of observing measurement outcome E_l on a single trial is $\Pr(E_l|\rho_k) = \text{Tr}(\mathcal{E}(\rho_k)E_l)$. The probability of observing all the recorded experimental data is given by the likelihood function:

$$L(\mathcal{E}) = \prod_{kl} \text{Tr}(\mathcal{E}(\rho_k)E_l)^{n_{kl}} \quad (6)$$

where n_{kl} is the number of times outcome E_l was observed when state ρ_k was prepared. We estimate the process using the method of maximum likelihood (ML), which involves maximizing the log-likelihood function $\mathcal{L}(\mathcal{E}) = \ln(L(\mathcal{E}))$ over all two-qubit completely-positive trace-preserving (CPTP) maps \mathcal{E} . We use the Choi matrix representation (41), in which the process \mathcal{E} is represented by the d^2 -by- d^2 density matrix $\chi = (I \otimes \mathcal{E})(|\Phi^+\rangle\langle\Phi^+|)$, where $|\Phi^+\rangle = \frac{1}{\sqrt{d}} \sum_{i=0}^{d-1} |i\rangle|i\rangle$ is a maximally entangled state between two copies of the ($d=4$)-dimensional two-qubit Hilbert space, and I is the identity matrix. In terms of the Choi matrix, the action of the process on an input state is given by $\mathcal{E}(\rho_k) = d \text{Tr}_1(\chi(\rho_k^\top \otimes I))$, where Tr_1 denotes a partial trace over the first subsystem and $^\top$ denotes transposition. The log-likelihood function is then given by

$$\mathcal{L}(\mathcal{E}) = \sum_{kl} n_{kl} \ln \left(d \text{Tr}(\chi(\rho_k^\top \otimes E_l)) \right) \quad (7)$$

We use the “ $R\rho R$ ” algorithm for processes (42) to find the Choi matrix $\hat{\chi}$ that maximizes the log-likelihood function. Throughout this section, a “hat” placed above the symbol for a physical quantity is used to denote a statistical estimate of that quantity. The *entanglement fidelity* (43) with respect to $U = \text{CNOT}$ is defined to be

$$F(\mathcal{E}, U) = \langle\Phi^+| (I \otimes U^\dagger) \chi (I \otimes U) |\Phi^+\rangle \quad (8)$$

From the ML-estimated process we obtain the ML entanglement fidelities $\hat{F}_{ML} = 0.858$ for Data Set 1 and $\hat{F}_{ML} = 0.851$ for Data Set 2.

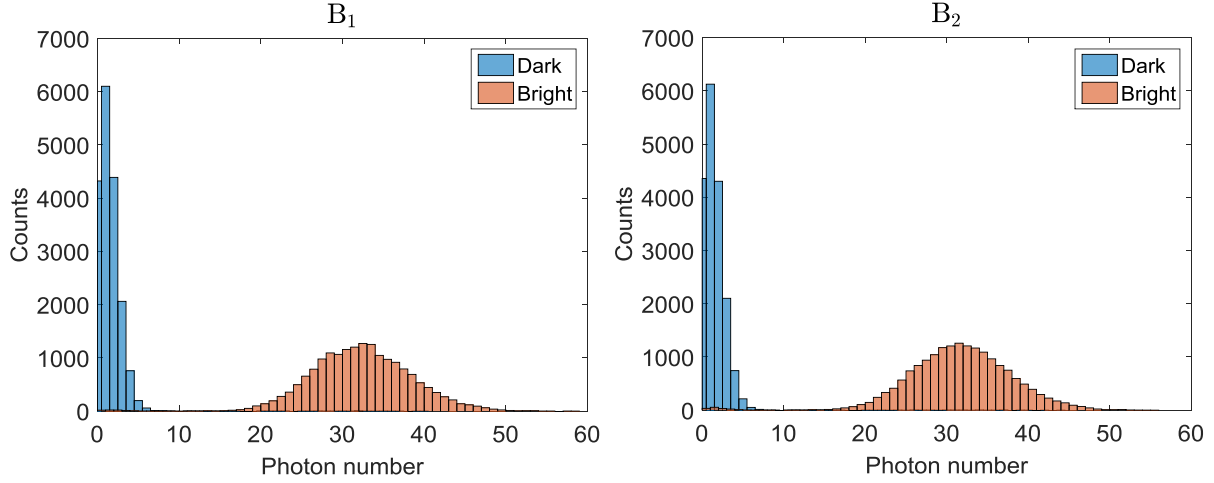


Figure S5: **Reference histograms.** Histograms of photon number counts when B ions are prepared in dark and bright states. Histograms are obtained from measurements taken during data acquisition. Photon count thresholds of 8 and 9 for B_1 and B_2 , respectively, are determined to minimize the probability of misclassification. The reference histograms are used to infer the single-qubit POVM element E_+ corresponding to observing a photon number greater than the threshold: $E_+ = (1 - p) |\text{Bright}\rangle_{\text{B B}} \langle \text{Bright}| + p |\text{Dark}\rangle_{\text{B B}} \langle \text{Dark}|$. We obtain $p = 0.0090$ and $p = 0.0134$ for B_1 and B_2 , respectively.

We obtain confidence intervals for the process fidelity using a parametric bootstrap method. Associated with each confidence interval is a confidence level. A confidence interval is defined as follows: in an ensemble of identically analyzed data sets (following the assumed model), one expects the frequency, with which the true value of the fidelity for any given data set will lie within that data set's confidence interval, to equal the confidence level. The ML estimate $\hat{\chi}$ is used to simulate 2000 synthetic data sets, and ML is run on each synthetic data set, producing a distribution of bootstrapped fidelities shown in Fig. S6. We then compute the basic bootstrap confidence interval (34), which is defined as follows: Let \hat{F}_{ML} be the ML estimated fidelity, and for $\alpha \in [0, 1]$, let f_α be the fidelity value corresponding to the $(100\alpha)^{\text{th}}$ percentile of the bootstrapped distribution. Then the $100(1 - 2\alpha)$ percent confidence interval is $[2\hat{F}_{ML} - f_{(1-\alpha)}, 2\hat{F}_{ML} - f_\alpha]$. The endpoints of the confidence interval are obtained by reflecting the

upper and lower percentile values of the bootstrapped distribution about the ML estimate. This results in a confidence interval that approximately corrects for bias in the ML estimate (see Fig. S6). Using this method, we obtain 95% confidence intervals of $[0.852, 0.878]$ for Data Set 1 and $[0.845, 0.872]$ for Data Set 2. Confidence intervals for other confidence levels are in Tab. S2.

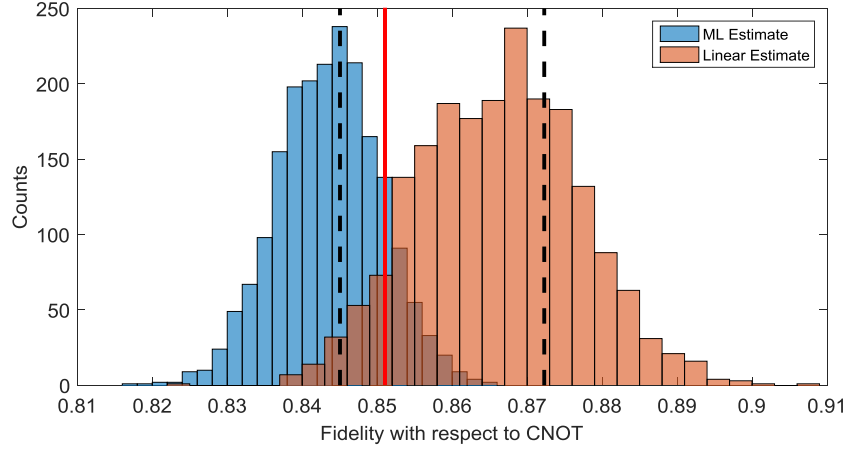


Figure S6: **Histograms of Bootstrapped Fidelity Distributions.** The blue (left) histogram displays the distribution of process fidelities obtained from running ML on 2000 parametric bootstrapped data sets generated from the ML estimated process $\hat{\chi}$ of Data Set 2. The red solid vertical line indicates the process fidelity of $\hat{\chi}$. The black vertical dashed lines mark the boundary of a 95% confidence interval computed via the basic bootstrap method. The orange (right) histogram displays the distribution of the linear fidelity estimator \hat{F}_L applied to 2000 non-parametric resamples of the experimental data set.

As a consistency check against the ML fidelity estimate, we also constructed a linear estimator \hat{F}_L that computes the fidelity directly from the observed frequencies: $\hat{F}_L = \sum_{kl} a_{kl} f_{kl}$, where f_{kl} is the observed frequency of seeing outcome E_l given state preparation ρ_k . To derive the coefficients a_{kl} , we first rewrite Eq. 8 as

$$F(\mathcal{E}, U) = \frac{1}{d^2} \sum_{i,j=0}^{d-1} \langle i | U^\dagger \mathcal{E}(|i\rangle\langle j|) U | j \rangle. \quad (9)$$

Since the set of input states and the set of POVM elements each form a complete operator basis, we can make the following expansions:

$$|i\rangle \langle j| = \sum_k b_k^{(ij)} \rho_k \quad (10)$$

$$U |j\rangle \langle i| U^\dagger = \sum_l c_l^{(ji)} E_l \quad (11)$$

Plugging back into Eq. 9, we get

$$\begin{aligned} F(\mathcal{E}, U) &= \frac{1}{d^2} \sum_{ij} \sum_{kl} b_k^{(ij)} c_l^{(ji)} \text{Tr}(E_l \mathcal{E}(\rho_k)) \\ &= \frac{1}{d^2} \sum_{ij} \sum_{kl} b_k^{(ij)} c_l^{(ji)} \text{Pr}(E_l | \rho_k) \end{aligned} \quad (12)$$

and therefore $a_{kl} = \sum_{ij} b_k^{(ij)} c_l^{(ji)}$. It remains to determine the coefficients $b_k^{(ij)}$ and $c_l^{(ji)}$. The set $\{E_l\}_l$ is an overcomplete basis, so there is a degeneracy of solutions to Eq. 11. We proceed as follows: let $|\rho_k\rangle\rangle$ be a vectorization of ρ_k and define the superoperator $\mathcal{S} = \sum_k |\rho_k\rangle\rangle \langle\langle \rho_k|$. Then the vectorized *dual basis* density matrix $\tilde{\rho}_k$ corresponding to ρ_k is defined by $|\tilde{\rho}_k\rangle\rangle = \mathcal{S}^{-1} |\rho_k\rangle\rangle$. The dual basis POVM elements \tilde{E}_l are defined analogously. Let $|ij\rangle\rangle$ be a vectorization of $|i\rangle \langle j|$. Then

$$\begin{aligned} |ij\rangle\rangle &= \mathcal{S} \mathcal{S}^{-1} |ij\rangle\rangle \\ &= \sum_k |\rho_k\rangle\rangle \langle\langle \rho_k| \mathcal{S}^{-1} |ij\rangle\rangle \\ &= \sum_k |\rho_k\rangle\rangle \langle\langle \tilde{\rho}_k| ij\rangle\rangle, \end{aligned} \quad (13)$$

and therefore a solution to Eq. 10 is given by $b_k^{(ij)} = \langle\langle \tilde{\rho}_k| ij\rangle\rangle = \langle j| \tilde{\rho}_k |i\rangle$. Similarly, a solution to Eq. 11 is given by $c_l^{(ji)} = \langle i| U^\dagger \tilde{E}_l U |j\rangle$. Plugging into Eq. 12 and after some simplification, we find that the coefficients in the linear estimator are given by

$$a_{kl} = \frac{1}{d^2} \text{Tr}(U \tilde{\rho}_k U^\dagger \tilde{E}_l). \quad (14)$$

Table S2: **Entanglement fidelities and confidence intervals.** Entanglement fidelities and confidence intervals of the teleported CNOT gate are determined using maximum likelihood (ML) estimation and linear estimator.

	Data set 1	Data set 2
Fidelity of ML process	0.858	0.851
Fidelity (68% CI from ML)	[0.858, 0.871]	[0.852, 0.866]
Fidelity (95% CI from ML)	[0.852, 0.878]	[0.845, 0.872]
Fidelity from linear estimator \hat{F}_L	0.871	0.866
Fidelity (68% CI from linear estimator)	[0.860, 0.882]	[0.856, 0.878]
Fidelity (95% CI from linear estimator)	[0.851, 0.892]	[0.845, 0.888]

The linear fidelity estimator is a consistent and unbiased estimator, meaning that \hat{F}_L converges to $F(E, U)$ in the limit of infinite trials per experiment and the expectation of \hat{F}_L is $F(E, U)$. However, \hat{F}_L has a larger variance than \hat{F}_{ML} , in part due to effects that occur at the boundary of quantum state space. We generate 2000 non-parametric bootstrapped data sets to obtain error bars on the linear fidelity estimate. The distribution of bootstrapped linear fidelity estimates is shown in Fig. S6. As \hat{F}_L is unbiased, its value for the experimental data approximately equals the mean of the bootstrapped distribution. Therefore the basic bootstrap confidence interval matches the interval between the corresponding quantiles of the distribution. We obtain a 95% basic bootstrap confidence interval of [0.845, 0.888] for \hat{F}_L , which contains the ML entanglement fidelity. The results from the ML estimation and the linear estimation of the two data sets are summarized in Table S2.

Pauli Transfer Matrix The ML-estimated process shown in Fig. 3 of the main text is in the Pauli transfer matrix representation. Let $\{P_i\}_{i=0}^{d^2-1}$ be an operator basis of n -qubit Pauli operators, where $d = 2^n$, and $P_0 = I$. Then the *Pauli transfer matrix* \mathcal{T} has entries $\mathcal{T}_{ij} = \frac{1}{d} \text{Tr}(P_i \mathcal{E}(P_j))$. The CPTP constraint on \mathcal{E} results in the properties that $\mathcal{T}_{00} = 1$, $\mathcal{T}_{0j} = 0$ for $j > 0$, and $-1 \leq \mathcal{T}_{ij} \leq 1$ for all i, j . The Pauli transfer matrix elements are related to the Choi

matrix by

$$\mathcal{T}_{ij} = \text{Tr}(\chi(P_j^\top \otimes P_i)). \quad (15)$$

Likelihood Ratio Test As a further consistency check, we perform a likelihood ratio test to investigate whether a CPTP map acting on a two-qubit state space is a good model for the observed data. The general problem of deciding between models to fit data is called model selection. For a recent reference on the use of model selection in quantum tomography, see (44). A model \mathcal{M} is a parametrized set of probability distributions. Given two nested models $\mathcal{M}_0 \subset \mathcal{M}_1$, the likelihood ratio test allows one to decide whether or not to reject the null hypothesis that the observed data is sampled from a distribution in the model \mathcal{M}_0 . In our case, let \mathcal{M}_0 denote the model of all probability distributions that could result from the application of a single CPTP map \mathcal{E} on each trial during the process tomography protocol. Let \mathcal{M}_1 denote the fully unrestricted model, that is, the set of all 144 independent probability distributions (one distribution for each combination of state preparation and measurement basis) on 4 elements. The *log-likelihood ratio statistic* λ is defined by

$$\lambda = 2(\mathcal{L}(\mathcal{M}_1) - \mathcal{L}(\mathcal{M}_0)), \quad (16)$$

where $\mathcal{L}(\mathcal{M}_0) = \max_{\mathcal{E}}(\mathcal{L}(\mathcal{E}))$ is the maximum of the log-likelihood function defined in Eq. 7, and $\mathcal{L}(\mathcal{M}_1) = \sum_{kl} n_{kl} \ln(p_{kl})$ is the maximum log-likelihood of the fully unrestricted model given the observed data.

Likelihood ratio tests often assume that λ has a chi-squared distribution, but because of boundary effects, this assumption is typically not true in quantum tomography experiments (44). Rather than using a chi-squared distribution, our likelihood ratio test compares the value of λ computed from the experimental data with the distribution of values for λ obtained from the bootstrapped data sets. Roughly, if the experimental value of λ is near the center of the bootstrapped distribution, then there is no statistical evidence for rejecting \mathcal{M}_0 . We quantify

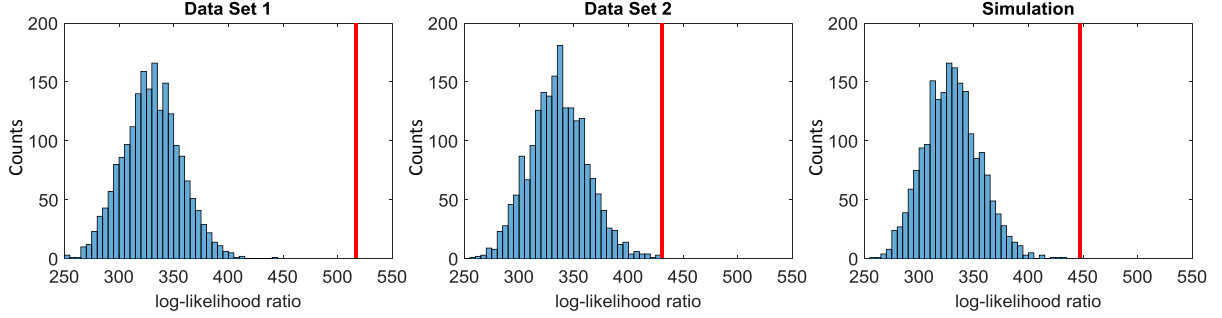


Figure S7: **Likelihood ratio tests.** Comparison of the log-likelihood ratio statistic λ defined in Eq. 16 with the distribution of values of λ obtained from 2000 parametric bootstrap resamples from the ML process. The deviation of the experimental value of λ from the distribution are 7.1, 3.6, and 4.6 standard deviations for Data Set 1, Data Set 2, and a simulated data set, respectively. The simulated data set results from a simulation of the experiment that models systematic errors caused by drifts in the B single-qubit rotation angle, as explained in the text.

model discrepancy as $(\lambda - \bar{\lambda})/\sigma$, where λ is obtained from the original data, and $\bar{\lambda}$ and σ are the mean and standard deviation of the log-likelihood ratio statistic from the bootstrap data sets. The results of the likelihood ratio test are shown in Fig. S7. We observe model discrepancy at the level of 7.1 and 3.6 standard deviations for Data Sets 1 and 2, respectively. This indicates that the data is inconsistent with the null model \mathcal{M}_0 in the sense that application of a single CPTP map to the specified input states followed by measurement by the inferred POVM does not fit the data as well as the fully unrestricted model. Such a discrepancy could be caused by context dependence, that is, a systematic dependence of the applied process on external variables (45).

A known systematic error present in the experiment is the drifts of Rabi rates for single-qubit rotations on the B ions. To investigate whether such drifts may be responsible for the observed model discrepancy, we simulated a data set with correlated over-rotation errors on the state preparation and measurement pulses as well as the single-qubit rotations when implementing the CNOT gates on B and M pairs shown in Fig. S2c. The magnitude of the errors in the

simulation drifts according to the pattern observed in Fig. S8. A likelihood ratio test on the simulated data set yields a discrepancy at the level of 4.6 standard deviations, as shown in Fig. S7. We conclude that a large portion of the model discrepancy observed in the experimental data can be explained by drifts in the rotation angles. The likelihood ratio test helped identify an error source in the experimental setup, which can be corrected with improvements to the apparatus. We believe this illustrates the importance of performing model consistency checks in addition to tomography when characterizing quantum processes.

To verify the existence of rotation-angle drifts for single-qubit rotations on B ions in the experimental setup, we performed a separate investigation in which we monitored the population of B ions after applying various numbers of $\pi/2$ pulses as shown in Fig. S8a. The deviation from the starting population was converted to fractional changes in rotation angles $\delta\theta/\theta$ (Fig. S8b), where θ is the target pulse area, and $\delta\theta$ is the deviation of the actual pulse area from the target value. A maximum fractional change of up to 4% was observed over a period of 4 hours in the measurement shown. The drifts are mainly caused by the relative power fluctuation between the two spatially overlapped laser beams used to drive the co-propagating carrier, although the total power of the two is actively stabilized. The power ratio between the two beams was about 1 : 3 at the time of the measurement. Balancing the power ratio between the two beams reduced the drifts of Rabi rates, but still left the drifts at the percentage level. This indicates that actively stabilizing the beat-note amplitude of the two beams will benefit future experiments.

Error Sources We use a depolarizing model to estimate the total error of the gate teleportation process. Assuming an error ϵ for the process \hat{U} , the density matrix after the process becomes

$$\rho \rightarrow (1 - \epsilon)\hat{U}\rho\hat{U}^\dagger + \epsilon \cdot \hat{I}/d \quad (17)$$

where d is the dimension of the Hilbert space for the process. Stepping through and applying this to the different processes in the full algorithm allows us to compute a predicted density

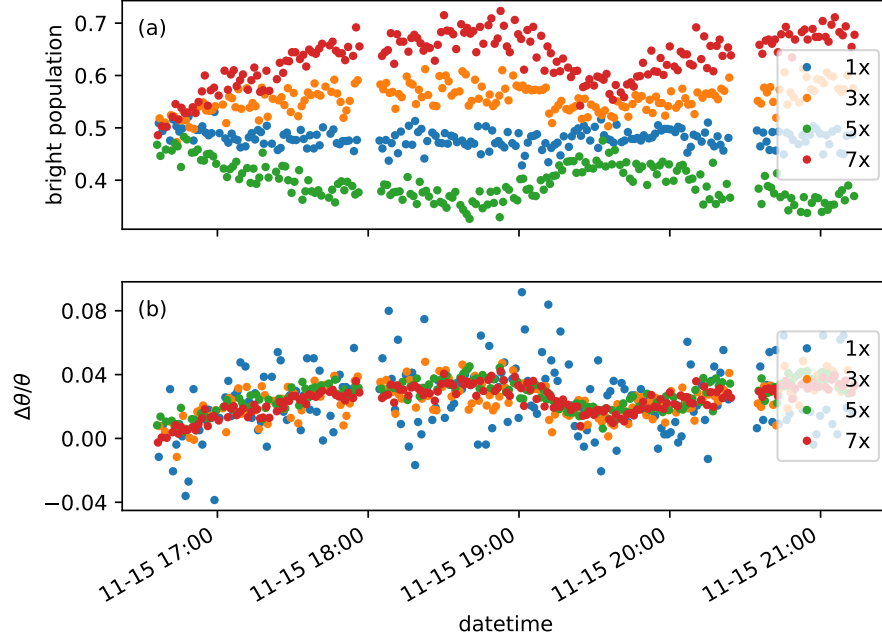


Figure S8: **Drifts of single-qubit-rotation pulses.** The rotation-angle drifts of single-qubit-rotations on B ions are measured by applying 1 (blue), 3 (orange), 5 (green), and 7 (red) $\pi/2$ pulses. The odd number of single-qubit-rotation pulses excite the population to around 0.5, therefore providing maximum sensitivity to rotation angle changes. Every single $\pi/2$ pulse takes approximately $10\ \mu\text{s}$ with about $40\ \mu\text{s}$ gap between the pulses. Data taken on June 15, 2018. (a) Bright population after single-qubit rotation pulses. (b) Fractional changes of rotation angles derived from measured population. (See text)

matrix after the complete teleportation process and derive the fidelity with respect to an ideal CNOT.

The error sources that we consider are SPAM errors on each qubit, the gate errors of each composite gate (Fig. S2), the error due to decoherence of the M ions, and depumping errors induced by stray resonant light.

The SPAM errors for the individual qubits are taken from SPAM diagnosis experiments (see Fig. S9a and S9b) interleaved with the tomography measurements. In the SPAM diagnosis experiments, for each ion we measure the probability $\epsilon_{X,\uparrow}$ of measuring the ion in $|\downarrow\rangle_X$ after

Table S3: **SPAM errors measurements.** The uncertainties are determined from the standard deviation of multiple measurements.

	$\epsilon_{X,\uparrow} (10^{-2})$	$\epsilon_{X,\downarrow} (10^{-2})$	$\bar{\epsilon}_X (10^{-2})$	$\epsilon_{X,\text{Bell}} (10^{-2})$
B ₁	0.5(4)	0.4(2)	0.5(2)	0.7(3)
B ₂	1(1)	0.4(2)	0.7(6)	1.0(9)
M ₁	0.2(1)	1.4(4)	0.8(2)	1.2(3)
M ₂	0.2(1)	1.3(3)	0.7(2)	1.1(3)
Two M ions (microwave)	0.2(1)	2.2(4)	1.2(2)	1.8(3)

preparing it in the $|\uparrow\rangle_X$ state, where $X = B_1, B_2, M_1$, or M_2 . We also measure the probability $\epsilon_{X,\downarrow}$ of measuring the ion in the $|\uparrow\rangle_X$ after preparing it in the $|\downarrow\rangle_X$ state. The “Map In” and “Map Out” pulses for these measurements are described in section State Preparation and Detection. We use the mean value $\bar{\epsilon}_X = \frac{\epsilon_{X,\uparrow} + \epsilon_{X,\downarrow}}{2}$ to estimate the SPAM errors for each qubit in the gate teleportation sequence. In addition, we also measured the SPAM errors of two M ions in a static well, using only microwave pulses for “Map In” and “Map Out”. These results are listed in Tab. S3 and used later to account for errors in individual gates.

We use the Bell-state fidelities from each composite two-qubit gate with the contribution from SPAM errors subtracted as a representative estimate of their process fidelities. When estimating the Bell state fidelity by measuring qubit populations and the contrast of parity oscillations (46), each qubit contributes an amount $\epsilon_{X,\text{Bell}} = \frac{3}{2}\bar{\epsilon}_X$ to the observed Bell state fidelity (47). After subtracting the contribution from SPAM errors, we estimate an infidelity of 0.040(9) for the Bell-state-generating gate \hat{F} , and 0.030(9) and 0.03(1) for the CNOT gates in the double-well potentials.

The error from M ion decoherence is estimated from the coherence time of a one-M Ramsey experiment. Here we account for the fact that the two M ions are in the Bell state for a duration of 4.2 ms and that a coherent superposition needs to be preserved in M_2 for a further 3.6 ms. We model this decoherence error as equivalent to the contrast reduction in the one-M Ramsey

sequence with a wait time of $2 \times 4.2 + 3.6 = 12$ ms. From the one-M $1/e$ coherence time of 140(30) ms, where the uncertainty represents day-to-day fluctuations from ambient noise, we estimate the error from M decoherence to be 0.007(3).

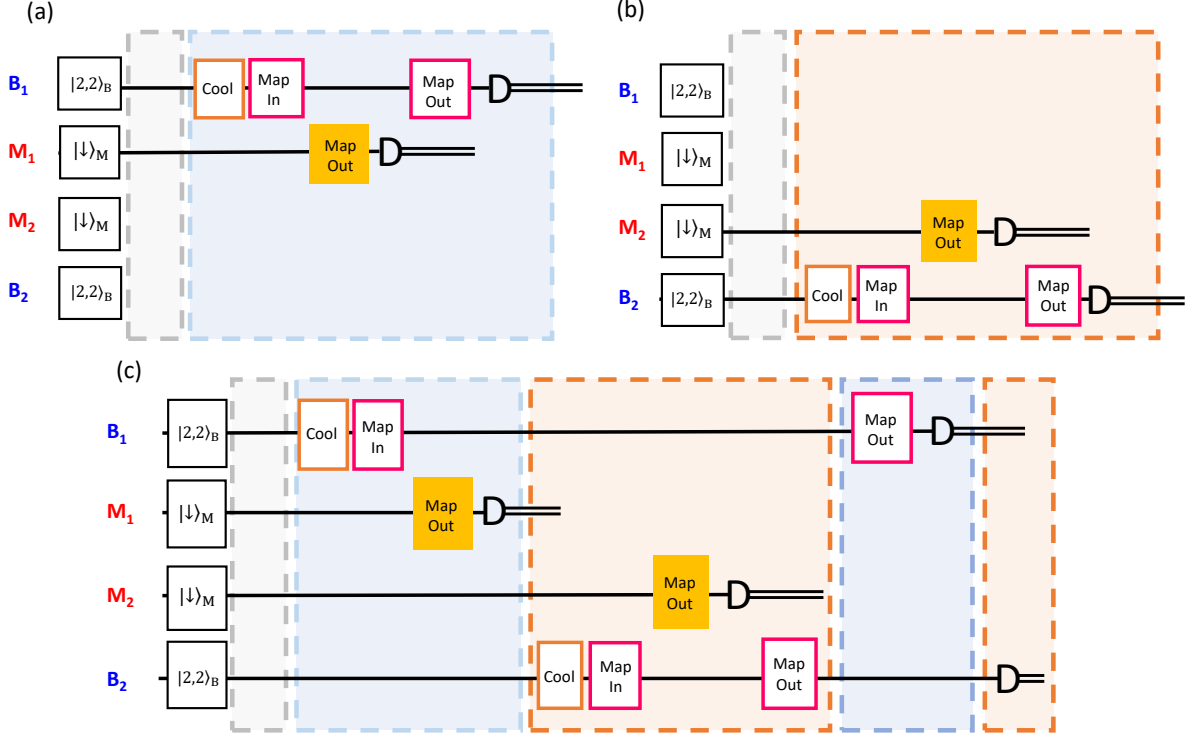


Figure S9: Experiments for determining SPAM and depumping errors. (a) and (b) Sequence for determining the SPAM errors for B and M ions detected in the double well potential. These are also the reference experiments for determining the stray-light-induced depumping errors. (c) To determine the stray-light-induced depumping error, cooling, state preparation, and measurement pulses are applied in the same order as in the gate teleportation sequence to conduct SPAM measurements for all four qubits. These measurements contain the SPAM errors plus the stray-light-induced depumping errors. The difference between this and the reference experiments in (a) and (b) gives the stray-light-induced depumping error.

We consider the errors from stray-resonant-light-induced depumping on ions outside of the LIZ. This is quantified as the difference between two SPAM experiments. A reference experiment measures the SPAM errors for one pair of B and M ions by shuttling the pair to the LIZ and

performing the measurement there (Fig. S9a,b). In a separate experiment, we perform shuttling, cooling, state preparation, and detection in the same order as in the gate teleportation experiment to measure the SPAM error plus the stray-light-induced depumping error (Fig. S9c). The difference of the two experiments is taken as the depumping error. We obtain errors of 0.011(4) for M_1 (due to the detection of M_2) and 0.012(3) for B_2 (due to cooling and repumping of B_1).

Based on the following assumptions and estimates, we can reject the hypothesis that the stray-resonant-light-induced depumping errors are induced solely by light scattering from the ions in the LIZ. Assuming a scattering rate of $R_1 = \gamma_M/2$ for the M_1 ion at the LIZ from a detection pulse with a duration of $\tau = 200 \mu\text{s}$, the M_2 ion away from the LIZ experiences an intensity of $I_2 \simeq \frac{\gamma_M}{2} \cdot \frac{hc}{\lambda_M \cdot 4\pi d^2}$ from the scattering, where γ_M is the linewidth of the upper state of M ions, h is the Planck's constant, c is the speed of light, λ_M is the wavelength of M resonant light, and $d = 340 \mu\text{m}$ is the minimum distance between the double well. Subject to the intensity I_2 , the M_2 ion will scatter at a rate $R_2 = \frac{I_2}{hc/\lambda_M} \sigma_M$ with $\sigma_M \simeq \frac{3}{2\pi} \lambda_M^2$ as the absorption cross section of M ions at resonance. This implies a scattering probability of about 6×10^{-4} during a detection period of $200 \mu\text{s}$, which is much lower than the observed error rate of a few percent.

Depumping errors on the order of one percent indicate that on average at least 0.01 photons are scattered in one experiment due to fluorescence detection at the LIZ. In comparison, ~ 1000 resonant photons are scattered by an ion in the bright state in the LIZ. This is approximately equivalent to an intensity ratio of $\sim 0.01/1000 = 10^{-5}$ between the resonant light intensity outside of the LIZ compared to the light intensity in the LIZ. Reaching the goal of 10^{-4} error rates for practical fault tolerant quantum error correction would then require an intensity ratio of $\sim 10^{-7}$. This presents a significant engineering requirement in future ion traps, but one that could be removed by completely eliminating the use of qubit resonant light and instead offloading all resonant operations to a separate species ancilla (25).

Including all error sources (Tab. 1, main text) in the depolarizing model, we derive a total infidelity of 0.12(1) for the gate teleportation algorithm. We derive the uncertainty of the total infidelity by applying the bootstrap to the depolarizing model, and use the experimentally determined uncertainties for individual contributions of error sources. The fidelity determined from the depolarizing model is near the upper limits of the 95% confidence intervals obtained by both ML and linear estimation, indicating that the major error sources are included in the error propagation model.

Other error sources, such as drifting experimental parameters, are not included in the depolarizing model. The drifts of preparation and measurement pulses can still lead to bias in process fidelity. For example, we determine by simulation that rotation-angle drifts of single-qubit rotations on B ions, uniformly distributed up to 5%, lead to an under-estimation of process fidelity by $\sim 1\%$.

References and Notes

38. J. P. Gaebler, *et al.*, High-fidelity universal gate set for $^9\text{Be}^+$ ion qubits, *Phys. Rev. Lett.* **117**, 060505 (2016).
39. C. Monroe, *et al.*, Resolved-Sideband Raman Cooling of a Bound Atom to the 3d Zero-Point Energy, *Physical Review Letters* **75**, 4011 (1995).
40. Y. Wan, F. Gebert, F. Wolf, P. O. Schmidt, Efficient sympathetic motional-ground-state cooling of a molecular ion, *Physical Review A* **91**, 043425 (2015).
41. M.-D. Choi, Completely positive linear maps on complex matrices, *Linear Algebra and its Applications* **10**, 285 (1975).

- 42. J. Fiurek, Maximum-likelihood estimation of quantum measurement, *Physical Review A* **64**, 024102 (2001).
- 43. B. Schumacher, Sending entanglement through noisy quantum channels, *Physical Review A* **54**, 2614 (1996).
- 44. T. L. Scholten, R. Blume-Kohout, Behavior of the maximum likelihood in quantum state tomography, *New Journal of Physics* **20**, 023050 (2018).
- 45. K. Rudinger, *et al.*, Probing context-dependent errors in quantum processors, *arXiv:1810.05651* (2018).
- 46. C. A. Sackett, *et al.*, Experimental entanglement of four particles, *Nature* **404**, 256 (2000).
- 47. C. Ballance, High-Fidelity Quantum Logic in Ca^+ , Thesis, University of Oxford (2014).